



# Enhanced mechanical performance of gradient-structured CoCrFeMnNi high-entropy alloys induced by industrial shot-blasting

Ming-Zhi Zhang, Kun Zhang, Kai-Kai Song\*, Xiao-Yu Zou, Wei-Dong Song, Ke-Feng Li\*, Li-Na Hu, Ze-Qun Zhang, Jürgen Eckert

Received: 27 May 2022 / Revised: 10 June 2022 / Accepted: 13 June 2022  
© Youke Publishing Co., Ltd. 2022

**Abstract** In this study, CoCrFeMnNi high-entropy alloys (HEAs) with a surface gradient nanostructure were produced using industrial shot blasting, which improved their mechanical properties compared to the untreated alloy. The severely plastically deformed (SPD) surface layer had a multi-scale hierarchical structure with a high density of stacking faults, deformation nanotwins, and amorphous domains. The depth of the SPD layer steadily increased as the shot-blasting time increased. The differences in the microhardness and tensile strength before and after shot-blasting demonstrated the significant effect of the SPD layer on the mechanical performance. The microhardness of the homogenized HEA was  $\sim 5$  GPa. In comparison, the maximum microhardness of the specimens after 20 min of shot blasting was  $\sim 8.0$  GPa at the surface. The yield strength also improved by 178%, and a large ductility of  $\sim 36\%$  was retained. Additional nanograin boundary, stacking fault, and twin strengthening within the gradient-

nanostructured surface layer caused the strength to increase. During tensile deformation, strain concentration began at the surface of the specimen and gradually spread to the interior. Thus, the gradient-nanostructured surface layer with improved strain hardening can prevent early necking and ensure steady plastic deformation so that high toughness is achieved.

**Keywords** High-entropy alloy; Shot blasting; Gradient structure; Mechanical property; Deformation mechanism

## 1 Introduction

High-entropy alloys (HEAs) with multiple principal elements occupy a substantial region of the multicomponent phase space and have attracted considerable research

---

M.-Z. Zhang, K.-K. Song\*  
Shenzhen Research Institute of Shandong University, Shenzhen 518057, China  
e-mail: songkai8297@gmail.com

K. Zhang  
CAS Key Laboratory of Microgravity (National Microgravity Laboratory), Institute of Mechanics, Chinese Academy of Sciences, Beijing 100190, China

K.-K. Song, W.-D. Song  
State Key Laboratory of Explosion Science and Technology, Beijing Institute of Technology, Beijing 100081, China

K.-K. Song, X.-Y. Zou  
School of Mechanical, Electrical and Information Engineering, Shandong University, Weihai 264209, China

K.-F. Li\*  
Guangdong Institute of Materials and Processing, Guangdong Academy of Sciences, Guangzhou 510650, China  
e-mail: yunxing0001@163.com

L.-N. Hu  
Key Laboratory for Liquid-Solid Structural Evolution and Processing of Materials (Ministry of Education), Shandong University, Jinan 250061, China

Z.-Q. Zhang, J. Eckert  
Erich Schmid Institute of Materials Science, Austrian Academy of Sciences, Leoben 8700, Austria

Z.-Q. Zhang, J. Eckert  
Department of Materials Science, Montanuniversität Leoben, Leoben 8700, Austria



interest [1–6]. In particular, face-centered cubic (fcc) HEAs (such as the representative Cantor alloy CoCr-FeMnNi) have been investigated extensively owing to their outstanding mechanical properties [5, 6]. However, they often exhibit insufficient yield strength (YS) and surplus ductility [7]. Various methods have been considered to improve the YS at the expense of ductility [8–10]. Notably, the alloying element method [11–16] has been shown to effectively increase the strength of Cantor HEAs. For example, the introduction of Al and/or Ti can induce the formation of body-centered cubic/B2 phases and  $L1_2$ -type or  $\sigma$  nanoprecipitates [14–16], which causes pronounced solute solution hardening and precipitation hardening. Alternatively, thermomechanical processing strategies have been designed to promote desirable mechanical properties [11–18]. For example, processing Cantor HEAs with additional C via high-pressure torsion enhances the strength and ductility synergy, and the ultimate strength can reach 2141 MPa [15, 19].

Furthermore, appropriate surface treatments such as shot peening, ultrasonic impact treatment, and deep rolling [10, 20–23] can evade the strength–ductility trade-off. When the surface layers experience severe plastic deformation (SPD), the specimens are exposed to spatially gradient plastic strains from the surface to the center, which results in a multi-scaled hierarchical dislocation structure [10, 20–23]. Moreover, SPD can induce compressive residual stresses and work hardening in the surface layers [22–24], improving mechanical performance.

However, most surface treatments based on SPD require expensive systems, complicated processing routes, or large workspaces, which are feasible for scientific research but not industrial manufacturing. Traditional shot-blasting is a low-cost technique widely used in industrial production. Thus, it is desirable to develop a facile method of improving the strength of HEAs by shot blasting for large-scale and low-cost industrial applications. Few studies have investigated the microstructural evolution and mechanical properties of shot-blasted HEAs. Therefore, this study will prepare and treat a representative Cantor HEA using shot blasting with different holding time. Thus, the correlation between the gradient microstructure and mechanical properties will be clarified.

## 2 Experimental

Ingots with a nominal composition of  $\text{Co}_{20}\text{Cr}_{20}\text{Fe}_{20}\text{Mn}_{20}\text{Ni}_{20}$  (at%) were prepared by arc-melting the constituent elements (purity > 99.9%) in a Ti-gettered high-purity Ar atmosphere. Specimens with dimensions of 50 mm × 20 mm × 1.4 mm were fabricated by custom suction casting. The specimens were homogenized at

1373 K for 24 h under an Ar atmosphere with furnace cooling. Then, they were sent for surface treatment using a Hook shot-blasting machine (Mingtai Jincheng Q377, cast steel balls with a diameter of ~ 0.4 mm, shot blasting quantity:  $2 \times 120 \text{ kg}\cdot\text{min}^{-1}$ ). Processing durations of 15 and 20 min were used, and the corresponding specimens were named S1 and S2, respectively.

The phase formation and microstructure were characterized using X-ray diffraction (XRD, Rigaku D/max-rB), laser scanning confocal microscope (LSCM, VK-X1000/X105), scanning electron microscope (SEM, ZEISS Sigma500) equipped with an electron backscattered diffraction (EBSD) system (Oxford Nordlys max3), and transmission electron microscope (TEM, Talos F200S G2). The surface roughness was measured using LSCM, and measurements were repeated at least three times for each specimen. TEM specimens were prepared using the focused ion beam (FIB, TESCAN LYRA3) lift-out method. High-resolution TEM (HRTEM) and selected area electron diffraction (SAED) were also used to analyze the severely deformed region.

A nano-indenter (Anton Paar, CSM-NHT<sup>2</sup>) was used to examine cross-sectional hardness profiles of the specimens from the top surface to the interior. The applied force increased to 5 mN at a loading rate of  $10 \text{ mN}\cdot\text{min}^{-1}$ , and the holding time was 10 s. Uniaxial tensile tests were performed using an electronic universal testing machine (SUNS, UTM5105) with a strain rate of  $1 \times 10^{-3} \text{ s}^{-1}$ . The dog-bone tensile specimen had gauge dimensions of 10 mm × 3 mm × 4 mm. The deformation strain distribution was recorded as tension was applied using the stereo digital image correlation (DIC, IMETRUM PCA1200) technique. The residual stress was measured using an X-ray stress analyzer (Rigaku, PSPC-MSF3M).

## 3 Results and discussion

### 3.1 Phase formation and microstructural features

LSCM images showing the surface morphologies of the homogenized and shot-blasted specimens, and corresponding cloud pictures describing the surface roughness are presented in Fig. 1. The surface of the homogenized specimen was smooth (Fig. 1a), whereas the surfaces of the shot-blasted specimens showed many microscale dimples caused by the high-velocity impacts of the steel balls (Fig. 1b, c) [25]. Figure 1d–f shows that the surface roughness increased after shot-blasting. The surface roughnesses of the homogenized, S1 and S2 specimens were approximately 1.45, 5.23 and 6.64  $\mu\text{m}$ , respectively. XRD observations (Fig. 2a) indicated that the as-cast and homogenized specimens consisted of a single fcc solid solution phase, which is consistent with previous reports

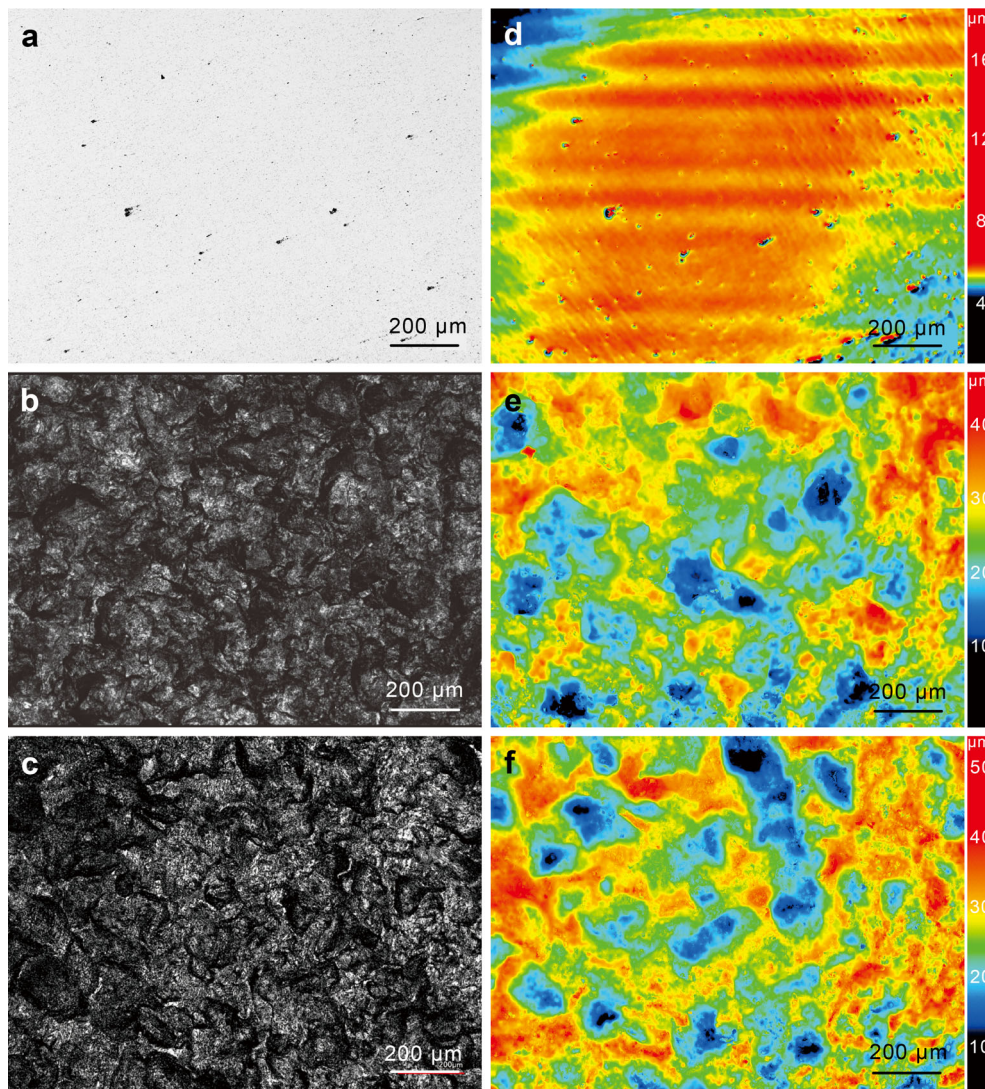


**Fig. 1** LSCM images of surface morphologies and corresponding cloud pictures related to surface roughness for **a, d** homogenized, **b, e** S1, and **c, f** S2 samples

[1–6]. As shown in Fig. 2b, c, completely recrystallized grains 40–500  $\mu\text{m}$  in diameter were observed in the homogenized specimen, and many straight-sided bands ran across the grains (i.e., annealing twins). This is a prominent microstructural feature of most annealed fcc metals and alloys [26]. In general, a large grain boundary velocity during long-term annealing favors the formation of annealing twins owing to growth accidents [26]. Moreover, the low stacking-fault energy (SFE) of Cantor alloys (i.e., 26–30  $\text{mJ}\cdot\text{m}^{-2}$  [27, 28]) also encourages the formation of annealing twins because growth accidents are more easily tolerated.

After shot-blasting, no phase transformations were detectable at the surface of the specimens. However, an apparent peak intensity variation was observed, the full

width at half maximum (FWHM) increased, and the intensity of the crystalline peaks decreased. For example, after shot blasting, the FWHM of the diffraction peak corresponding to the (111) crystallographic plane increased from  $(0.21 \pm 0.05)$  to  $(0.52 \pm 0.05)$  and the corresponding intensity decreased from  $(457 \pm 25)$  to  $(231 \pm 25)$  (Fig. 2d). These changes may be caused by the formation of residual stresses and/or nanocrystallization within the surface layer. Figure 2e shows the residual stress distribution over the depth of the shot-blasted S2 specimen. The residual stress induced by shot-blasting is compressive, so it has a negative value (Fig. 2e). The maximum compressive residual stress was  $(372.3 \pm 10.5)$  MPa, and it occurred 5  $\mu\text{m}$  from the top surface. In general, the absolute residual stress decreased as the depth increased.

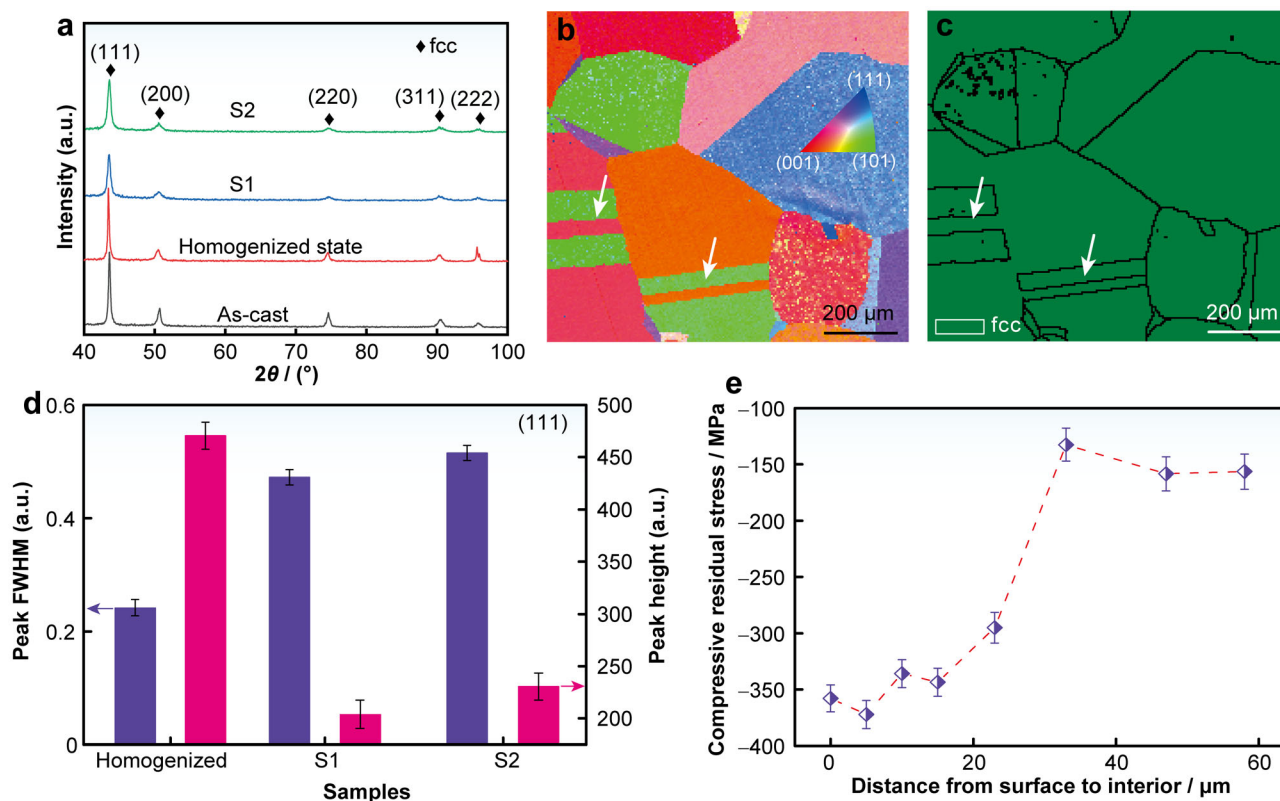


**Fig. 2** a XRD patterns of all investigated samples together with cast samples; EBSD b inverse pole figure (IPF) map and c phase map of homogenized samples; d FWHM of diffraction peak related to (111) crystallographic plane and intensity with increasing shot-blasting duration; e plot of residual stress vs. distance from surface to interior

However, nanocrystallization within the surface layers of the shot-blasted specimens should not be ignored. This is because repeated high-speed impacts on the surface of metallic materials can produce severe compressive deformation, transforming coarse grains near the surface to micro- or even nanograins [29, 30]. The shot-blasted specimens were analyzed using SEM, TEM, and HRTEM (Figs. 3, 4, 5). As expected, the affected areas exhibited a gradient microstructure as the impact energy from shot blasting gradually decreased from the surface to the interior.

Figure 3 shows the microstructures near the surface of the shot-blasted specimens. In comparison to the homogenized specimen, they showed severe deformation. The depth of the severely deformed surface was between 10 and 22  $\mu\text{m}$  in S1 (double-headed arrows in Fig. 3a), and 90 and 310  $\mu\text{m}$  in S2 (double-headed arrows in Fig. 3c). At higher magnification (arrows in Fig. 3b, d), many slip bands were observed. During shot blasting, steel balls struck the surface of the specimens with different incident angles, which caused dislocations and slip bands to propagate. Typical fcc structures have  $\{111\} \langle 110 \rangle$  slip systems, i.e., there are three  $\langle 110 \rangle$  directions for each of the four  $\{111\}$  slip planes [6]. However, the compression deformation

during shot blasting was not uniaxial or continuous, so subsequent impacts could crook previously formed slip bands. The density of the slip bands decreased as the depth from the surface increased. Therefore, the microstructures in the interior were less affected, and a multi-scale hierarchical dislocation structure was produced (Fig. 3e, f). Furthermore, as the shot blasting duration increased from 15 to 20 min, the surface layer experienced more significant strain. The deformation process propagated and gradually affected the interior of the specimen. Thus, the gradient nanograin structure became more apparent over time. Furthermore, as shown in Fig. 3f, nanosized deformation twins appeared during shot blasting. Hence, both microscopic residual stress stored within the highly deformed layer and grain refinement are believed to have caused the broadening of the XRD peaks.

To verify the nanograin gradient structure and the existence of twins and dislocations within the highly deformed layer, TEM and SAED were used to examine specimen S2 (Fig. 4). The bright- and dark-field TEM images (Fig. 4a, b) showed strong evidence of nanograin formation (e.g., dotted circles), and the SAED patterns confirmed the development of nanoscale fcc-type structures with no other phases (Fig. 4c). Furthermore,

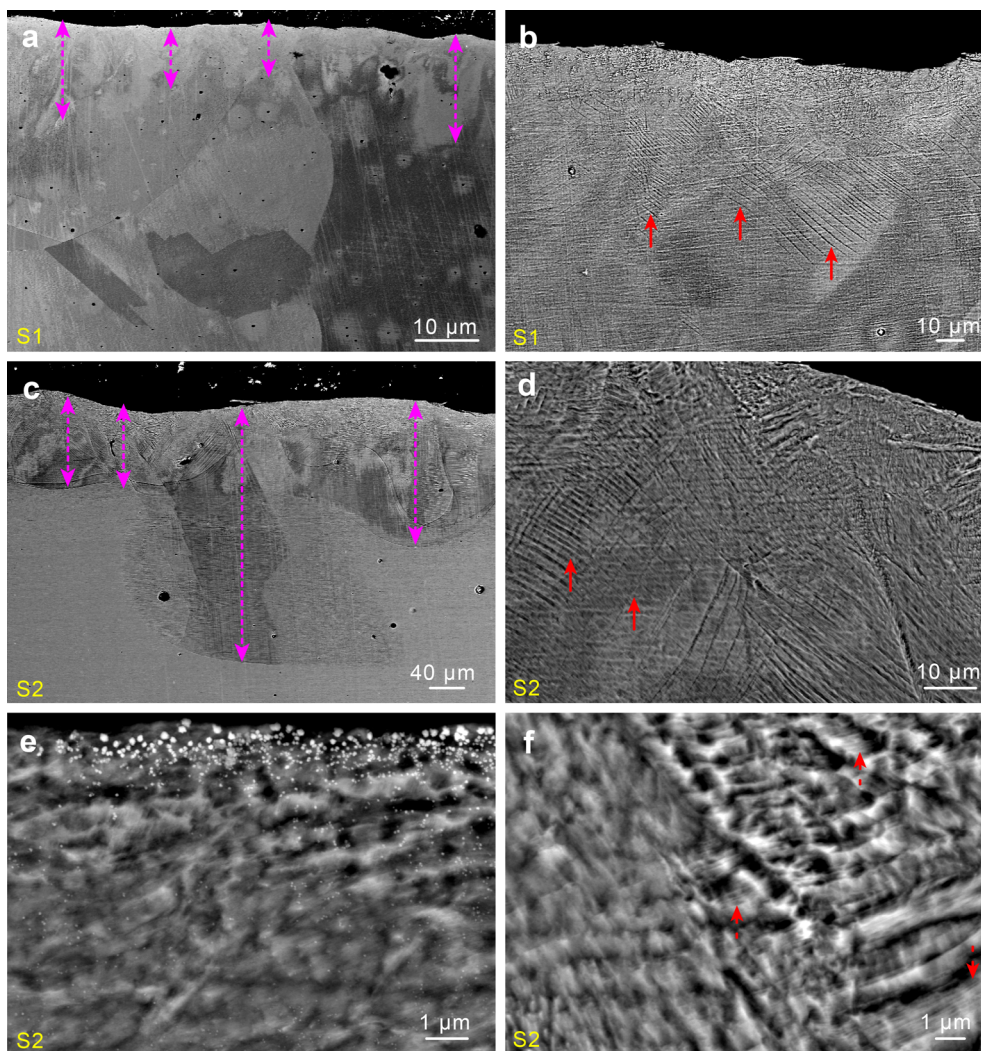


Fig. 3 SEM images of a, b S1 and c–f S2 samples after shot-blasting

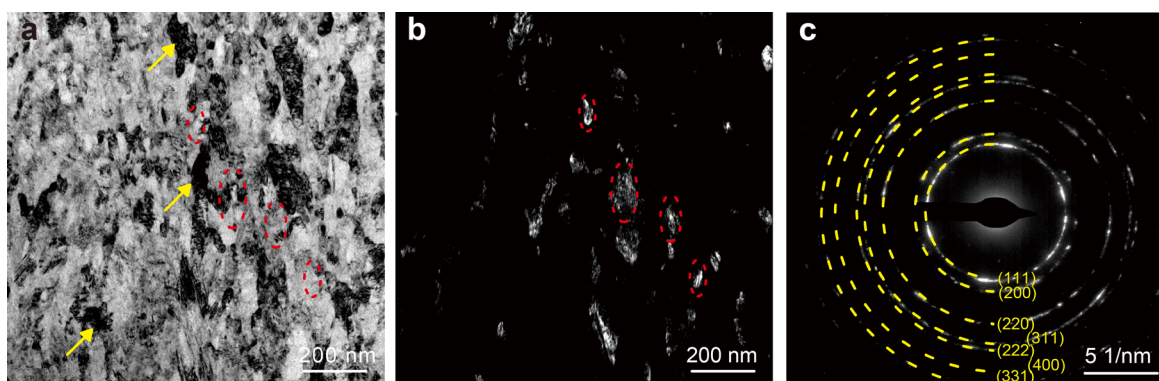
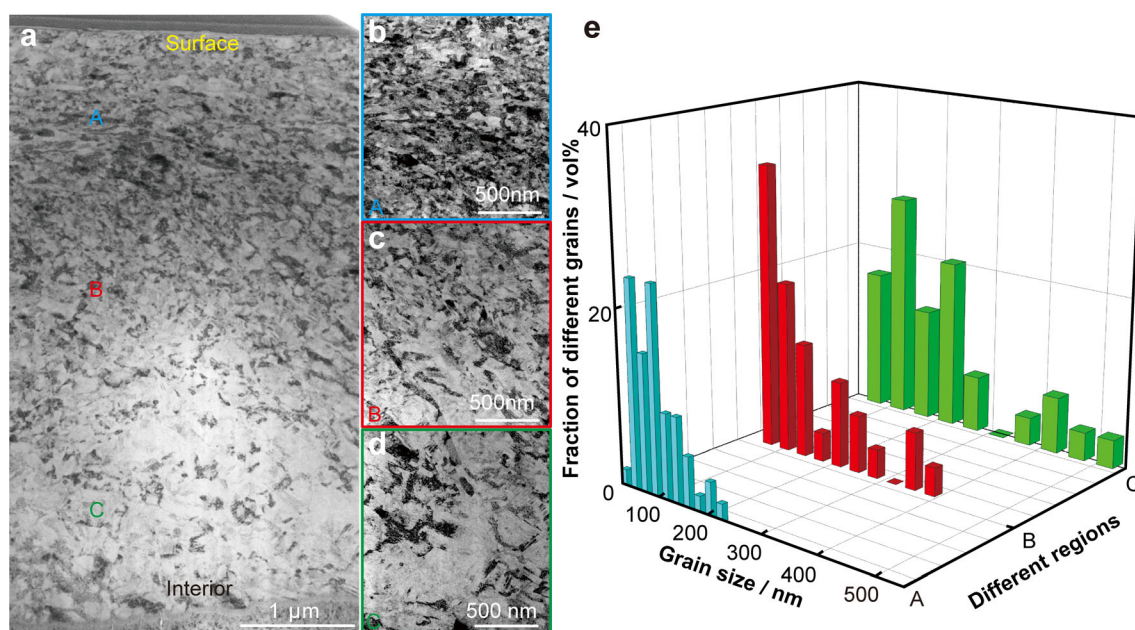


Fig. 4 a Bright-field and b dark-field TEM images and c corresponding SAED patterns of surface regions for S2 samples

numerous dislocations (see arrows) appeared within the nanograins around the grain boundaries. The evolution of the gradient microstructure from the surface to the interior of the highly deformed layer is shown in Fig. 5a. The grain

size gradually decreased as the depth into the shot-blasted specimen increased. A representative statistical analysis of the grain size was performed for Regions A, B and C from the top surface to the interior (Fig. 5b–d). The



**Fig. 5** a TEM images related to gradient microstructural evolution from surface to interior within highly deformed layer for S2 samples; b–d amplified images of Regions A, B and C marked in a; e distribution statistics of grain sizes performed on different regions

corresponding grain size distributions are shown in Fig. 5e. Compared to the grain size of the homogenized specimen (40–500  $\mu\text{m}$ ), extreme grain refinement was detected at the surface of the specimen after 20 min of shot blasting. The average grain sizes for Regions A, B and C were approximately 98, 150 and 197 nm, respectively, which further confirms the formation of a gradient nanograin microstructure. The formation of nanocrystalline microstructures through SPD of the surface layer during shot blasting is similar to that occurs during surface mechanical attrition treatment, for which the grain refinement mechanisms have reported [29]. In general, the Cantor CoCrFeMnNi alloy has a low SFE. This inhibits dislocation cross-slipping, but facilitates the formation of planar defect arrays, such as stacking faults (on the primary  $\{111\}$  slip planes) and deformation twins [31–33].

Further characterization of the deformed microstructure at the top surface of shot-blasted specimen S2 was conducted using HRTEM. A high density of stacking faults was observed (Fig. 6a). The applied strain and strain rate accumulated during shot blasting, and intersecting stacking faults within the homogenized grains transformed into sub-grain boundaries that subdivided coarse grains into fine ones. Moreover, twinning caused by the emission of Shockley partial dislocations from grain boundaries was identified, as shown in Fig. 6b, and the nanotwins were very small, typically less than 10 nm. Twinning is believed to be another crucial grain refinement mechanism for fcc metallic alloys with low SFEs [29, 34, 35]. The introduced twin boundaries (Fig. 6c) and twin–twin intersections are

high-angle boundaries that produce refined blocks within coarse grains and act as strong barriers to dislocation motion, thus, they provide Hall–Petch type strengthening [29, 34, 35].

The low SFE favors strain-induced phase transformations, introducing phase boundaries as an additional grain-refinement mechanism in HEAs [31–33]. Although no phase transformations were detected in this study, nanoscale amorphous structures (Fig. 6d), randomly distributed among crystalline nanograins, can be regarded as a second phase that provides an additional interfacial barrier to resist deformation. It is well established that amorphization in metallic materials can occur through rapid solidification [36] or by destabilization of a crystalline solid phase into a disordered one [37]. It is common for crystal structures to transform into an amorphous phase through SPD [38, 39]. Applying a high strain and strain rate increases the severity of lattice distortion and promote the formation of amorphous structures [40]. For Cantor HEAs, SPD can induce the formation of concentrated deformation regions, which contain dislocations, stacking faults, and twins that serve as precursors to amorphization [41, 42]. Considering dislocations as an example, SPD usually introduces a high density of dislocations (between  $1 \times 10^{17}$  and  $1 \times 10^{18} \text{ m}^{-2}$ ), which act as precursors for amorphization [37–39]. For Cantor HEAs, the critical dislocation density for crystalline-to-amorphous transformations is approximately  $5.6 \times 10^{17} \text{ m}^{-2}$  [43]. In this study, the dislocation density was approximated using XRD patterns, which yielded a value of  $1.12 \times 10^{18} \text{ m}^{-2}$ . Thus, shot-blasting of

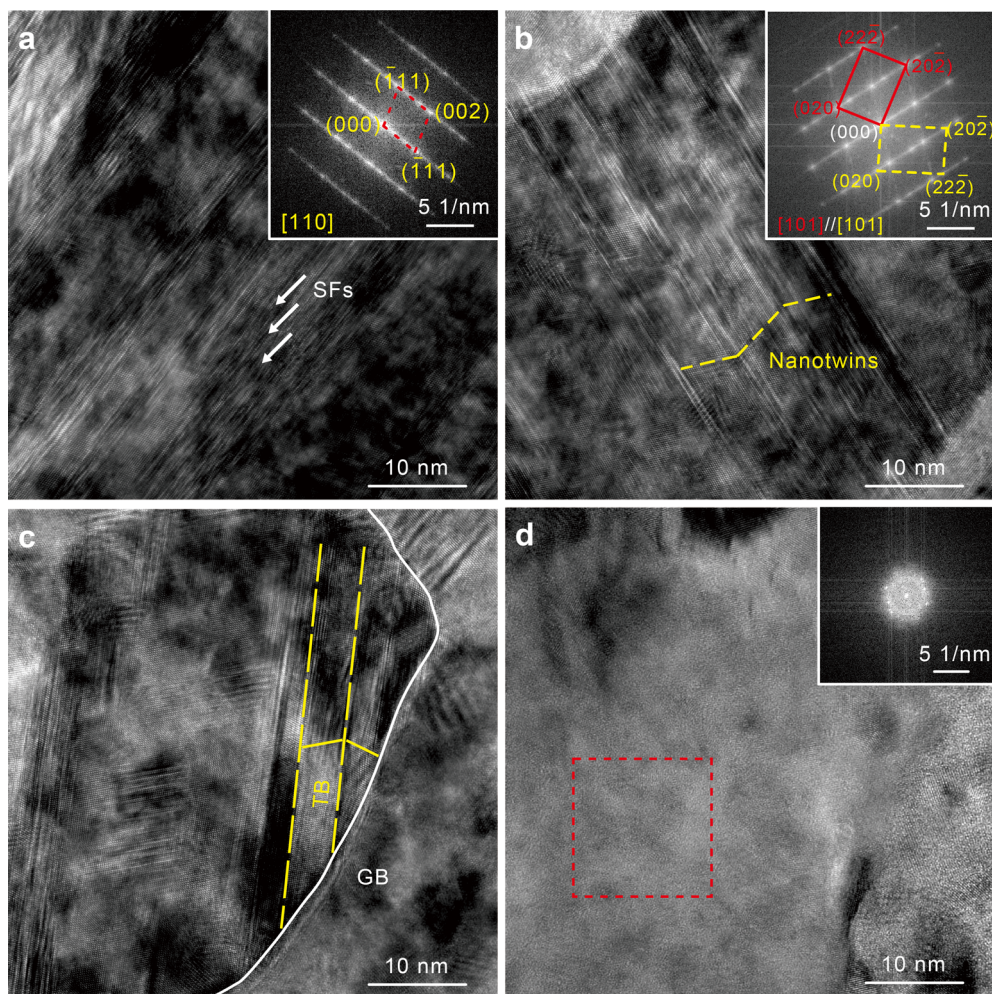


**Fig. 6** HRTEM images of **a** stacking faults, **b** nanotwins, **c** twin boundary (TB) and grain boundary (GB), and **d** amorphous phase within highly deformed layer for S2 samples

the CoCrFeMnNi HEA can introduce nanocrystalline microstructures by subdivision of grains via dislocations, stacking faults, and deformation twins. Moreover, it can facilitate solid-state amorphization to create phase boundaries that enhance the matrix.

### 3.2 Mechanical properties and deformation mechanisms

Miniaturized surface microstructures increase the free-surface fraction such that it has a dominant effect on the overall mechanical properties of the materials. The nanoindentation hardness was measured before and after shot blasting. Figure 7a shows the trends in the hardness from the top surface to the interior of the specimens. The hardness increased significantly as the shot-blasting time increased. The maximum hardness was  $\sim 8.0$  GPa, which occurred at the surface and gradually decreased towards the interior. At a depth of  $\sim 13$   $\mu\text{m}$ , the hardness decreased to

5.5–6.2 GPa, which is comparable with the homogenized specimen. The shot-blasting-induced hardening near the surface can be attributed to the variation in deformation twins and dislocations, whose gradient distribution is substantially affected by processing parameters such as the blasting time.

Tensile experiments were conducted to further analyze the mechanical properties of the shot-blasted Cantor HEA, and the results are summarized in Table 1. Compared to the homogenized specimen, the shot-blasted specimens showed significant improvements in YS ( $\sigma_{0.2}$ ) and ultimate tensile strength (UTS,  $\sigma_{\text{UTS}}$ ) (Fig. 7b). The homogenized specimen exhibited a plastic strain ( $\epsilon_p$ ) of approximately 53%, and the YS and UTS were  $(153 \pm 15)$  MPa and  $(477 \pm 10)$  MPa, respectively. After 15 min of shot blasting, the YS and UTS both increased to  $(310 \pm 15)$  MPa and  $(536 \pm 10)$  MPa, respectively, and there was an insignificant decrease in ductility ( $\epsilon_p \approx 48\%$ ). When the shot-blasting time was increased to

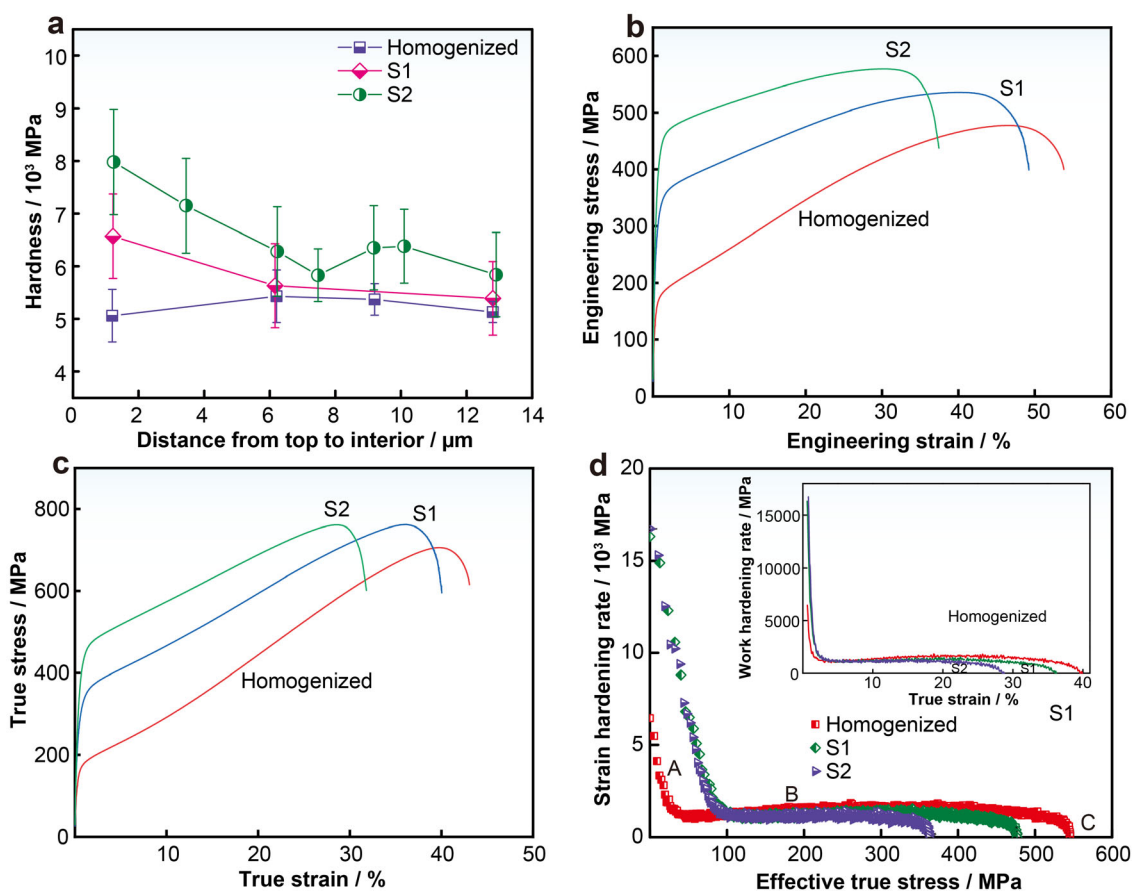


**Fig. 7** a Hardness results before and after shot blasting treatments, b engineering stress–strain curves, c true stress–strain curves, and d strain hardening rate for investigated samples and inset being work-hardening rate vs. true strain curves for investigated samples

**Table 1** Yield strength, ultimate tensile strength, and plastic strain of investigated samples

Sample	$\sigma_{0.2}$ / MPa	$\sigma_{UTS}$ / MPa	$\varepsilon_p$ / %
Homogenized	$153 \pm 15$	$477 \pm 10$	$53 \pm 3$
S1	$310 \pm 15$	$536 \pm 10$	$53 \pm 3$
S2	$426 \pm 15$	$577 \pm 10$	$53 \pm 3$

20 min, the YS increased substantially to  $(426 \pm 15)$  MPa, and the UTS increased to  $(577 \pm 10)$  MPa. Meanwhile, the plastic strain decreased from approximately 53% to 36%.

The true stress–strain curves and corresponding strain hardening rates for all the specimens are shown in Fig. 7c, d, respectively. Both plots show three distinct stages: A, B, and C. The plot of the strain-hardening rate ( $d\sigma/d\varepsilon$ ) against the effective true stress ( $\sigma - \sigma_{0.2}$ ), commonly called a Kocks–Mecking (KM) plot, can be used to characterize differential variations of structures experiencing stress–strain [44]. All the specimens exhibited a rapid decrease in

the strain-hardening rate in Stage A, which was probably caused by the transition from the elastic to the elastic–plastic stage [45, 46]. Then, in Stage B, the strain-hardening rate stabilized, and the plots show an extremely weak bulge. This was probably caused by mutual competition between dislocation pile-ups, twins, stack faults, and softening from slip bands [1, 7, 47]. Stage C was characterized by a continuously decreasing strain-hardening rate, which can be linked to damage processes such as void formation, initiation, and microcrack propagation [44].

Figure 8 shows the fracture morphologies of the specimens after tensile deformation. The cross-sectional fracture images show many dimples, which confirms that all the specimens exhibited ductile fracture behavior regardless of their processing route (Fig. 8a–c). At higher magnification, the homogenized specimens with the highest ductility showed a lot of very large deep dimples and a few small shallow dimples. After shot-blasting, the number, diameter, and depth of the large deep dimples decreased (Fig. 8d–f). In contrast, the number of small shallow dimples increased. In general, the size of the dimples is highly dependent on the ductility of the metallic alloy, i.e., specimens with

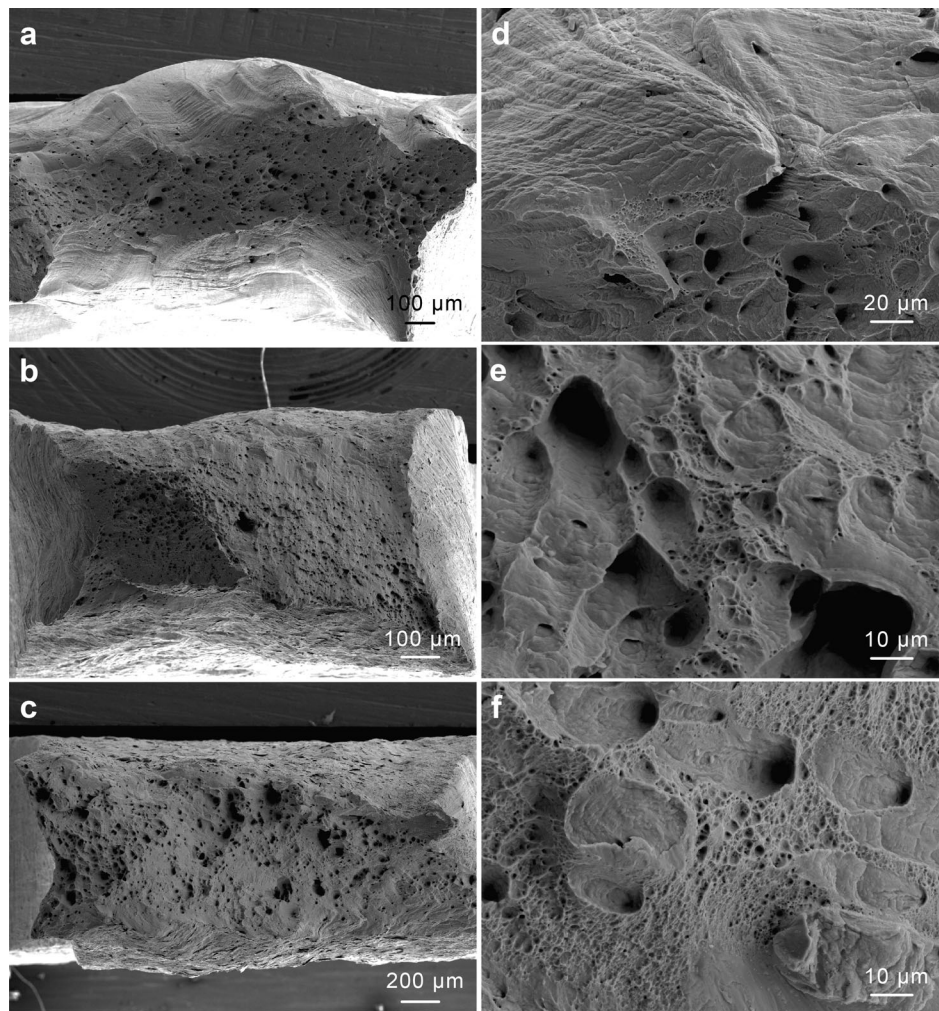


**Fig. 8** SEM images related to fracture morphologies and their corresponding amplified images for **a, d** homogenized, **b, e** S1, and **c, f** S2 samples

better ductility exhibit larger dimples, which is in accord with our tensile measurements.

In recent years, the deformation mechanisms of Cantor HEAs have been investigated systematically [1, 3, 6, 7, 46]. During deformation, initial yielding occurs owing to simple planar slipping of the  $\frac{1}{2} \langle 110 \rangle$  dislocations, which are often separated into Shockley partials, on the  $\{111\}$  slip planes. Upon further deformation, dislocations build up at the grain boundaries and induce secondary slipping. This leads to dislocation intersections and increases the number of obstacles to slipping. Thus, extensive dislocation tangles and forest dislocations can be observed [1, 3, 6, 7, 46]. In other words, during the deformation of Cantor HEAs at room temperature, the dislocation substructure evolves from planar slipping at minor strains to cross-slipped tangled dislocations at intermediate strains and cell structures at high strains [1, 3, 6, 7, 46]. Furthermore, deformation twins occur alongside dislocation multiplication and interactions. However, during plastic deformation at room

temperature, deformation twins are only activated close to the fracture strain because the relatively low YS of Cantor HEAs means that higher strains are required to induce twinning stress through work hardening [46, 47]. Hence, twinning does not substantially affect tensile deformation at room temperature [46, 47].

Shot-blasting surface treatment leads to the formation of a gradient nanostructured surface layer that contains nanoscale fcc grains, stacking faults, deformation twins, and an amorphous phase. Thus, the deformation mechanisms of treated specimens should differ from those of homogenized specimens. The gradient microstructure means that the interior should be deformed initially, whereas the gradient surface layer remains elastic during elastic–plastic deformation [48]. With further deformation, the interior cannot deform freely owing to the limitations of the elastic surface layer; thus, the interior and gradient surface layer are subjected to lateral tensile and compressive stresses, respectively [49]. Consequently, more slip

systems are activated, which aggravates dislocation activities. The deformation mechanisms in the interior should be similar to those of the cast specimens, but the resistance to dislocation activities is different. However, during plastic deformation, the plastic instability of the surface grains is strongly affected by complicated stress states owing to the constraints of the interior and residual stresses from shot blasting [48, 50]. These complicated stress states can induce different strain distributions during deformation. Strain distribution maps for the homogenized and S2 specimens under tension are presented in Fig. 9. At an applied strain of 15%, the homogenized specimen showed no apparent strain concentration along the tensile direction (Fig. 9a). At 20% strain, strain concentration occurred simultaneously in the surface layer and interior. However, for the S2 specimen, strain concentration began at the surface (white arrows in Fig. 9b). When the applied strain increased to 15%, the strain concentration at the surface intensified and then propagated into the interior, which led to the formation and propagation of catastrophic microcracks. Therefore, the strain maps of the specimens under tension demonstrate that the gradient-structured surface layer is responsible for the increased YS and UTS of the shot-blasted specimens.

Based on the microstructural observations, the strength can be approximated as [51]:

$$\sigma = \sigma_0 + \frac{k}{\sqrt{d_{fp}}} + \alpha Gb\sqrt{\rho} \quad (1)$$

where  $\sigma$  is the strength,  $\sigma_0$  is the friction stress,  $k$  is the Hall–Petch constant,  $d_{fp}$  is the mean free path for dislocations,  $\alpha$  is a constant,  $G$  is the shear modulus,  $b$  is the Burgers vector, and  $\rho$  is dislocation density. In general, conventional grain boundaries act as strong barriers to dislocation motion, providing Hall–Petch type strengthening [35]. Furthermore, deformation twins induced by shot

blasting offer new twin boundaries that strengthen the material through the so-called “dynamic Hall–Petch effect” [7]. A high density of nanograin boundaries, stacking faults, and amorphous phase boundaries can also impede dislocation movement during tensile deformation, known as Taylor hardening [7]. For example, the interfaces between deformation-induced amorphous bands and the fcc matrix provide strong barriers to dislocation motion and natural sinks for dislocations [42]. Therefore, the effects induced by shot blasting drastically decrease  $d_{fp}$  and increase  $\rho$ , which significantly increases the overall strength.

#### 4 Conclusion

In this study, the CoCrFeMnNi HEA (Cantor alloy) was subjected to shot blasting, and the resultant microstructure and mechanical properties were investigated. The shot-blasting treatment did not cause detectable phase transformations, and only one fcc phase was detected in the SPD surface layer and interior of the specimens. However, the treatment did induce high strains at high strain rates and led to the formation of gradient nanostructured surface layers containing refined nanograins, a high density of stacking-faults/dislocations, and deformation nanotwins as well as a certain amount of nano-amorphous phase.

Microhardness and tensile tests showed that shot blasting can substantially improve the mechanical performance of CoCrFeMnNi HEA. Compared to the homogenized HEA, the maximum microhardness after 20 min of shot blasting was  $\sim 8.0$  GPa, and the YS increased by 178%. The gradient-nanostructured surface layer with strain hardening can resist higher strain concentrations during the initial stages of deformation, preventing early necking and ensuring steady plastic deformation.

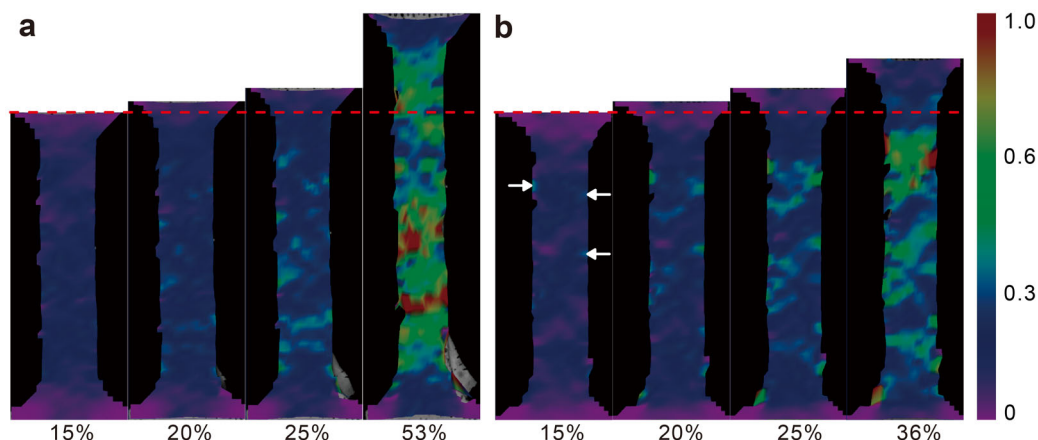


Fig. 9 Strain distribution maps of **a** homogenized and **b** S2 samples during tension

**Acknowledgements** The authors are grateful to K.L. Wang and Y.Q. Xin for their technical assistance on behalf of the Physical-Chemical Materials Analytical and Testing Center of Shandong University at Weihai. This research was financially supported by Shenzhen Science and Technology Program (No. JCYJ20210324121011031), the National Natural Science Foundation of China (Nos. 51871132 and 51971120), the Free Exploring Basic Research Project of Shenzhen Virtual University Park (No. 2021Szvup069), the Opening Project of the State Key Laboratory of Explosion Science and Technology (Beijing Institutes of Technology) (No. KFJJ21-08M), and the Natural Science Foundation of Shandong Province (No. ZR2020ME002).

## Declarations

**Conflicts of interests** The authors declare that they have no conflict of interests.

## References

- [1] Li Z, Zhao S, Ritchie RO, Meyers MA. Mechanical properties of high-entropy alloys with emphasis on face-centered cubic alloys. *Prog Mater Sci.* 2019;102:296. <https://doi.org/10.1016/j.pmatsci.2018.12.003>.
- [2] Zhang Y. *High-Entropy Materials*. 1st ed. Singapore: Springer Nature Singapore Pte. Ltd; 2019. 33. <https://doi.org/10.1007/978-981-13-8526-12021>.
- [3] George EP, Curtin WA, Tasan CC. High entropy alloys: a focused review of mechanical properties and deformation mechanisms. *Acta Mater.* 2020;188:435. <https://doi.org/10.1016/j.actamat.2019.12.015>.
- [4] Yeh JW, Chen SK, Lin SJ, Gan JY, Chin TS, Shun TT, Tsau CH, Chang SY. Nanostructured high-entropy alloys with multiple principal elements: novel alloy design concepts and outcomes. *Adv Eng Mater.* 2004;6:299. <https://doi.org/10.1002/adem.200300567>.
- [5] Cantor B, Chang ITH, Knight P, Vincent AJB. Microstructural development in equiatomic multicomponent alloys. *Mater Sci Eng A.* 2004;375:213. <https://doi.org/10.1016/j.msea.2003.10.257>.
- [6] Cantor B. Multicomponent high-entropy Cantor alloys. *Prog Mater Sci.* 2021;120:100754. <https://doi.org/10.1016/j.pmatsci.2020.100754>.
- [7] Otto F, Dlouhý A, Somsen C, Bei H, Eggeler G, George EP. The influences of temperature and microstructure on the tensile properties of a CoCrFeMnNi high-entropy alloy. *Acta Mater.* 2013;61:5743. <https://doi.org/10.1016/j.actamat.2013.06.018>.
- [8] Yu H, Li HB, Feng H, Li K, Tian Y, Jiang ZH. Enhancing the strength and ductility of CoCrFeMnNi high-entropy alloy by nitrogen addition. *Mater Sci Eng A.* 2020;789:139587. <https://doi.org/10.1016/j.msea.2020.139587>.
- [9] Klimova MV, Shaysultanov DG, Zherebtsov SV, Stepanov ND. Effect of second phase particles on mechanical properties and grain growth in a CoCrFeMnNi high-entropy alloy. *Mater Sci Eng A.* 2019;748:228. <https://doi.org/10.1016/j.msea.2019.01.112>.
- [10] An Z, Mao S, Liu Y, Zhou H, Zhai Y, Tian Z, Liu C, Zhang Z, Han X. Hierarchical grain size and nanotwin gradient microstructure for improved mechanical properties of a non-equiatomic CoCrFeMnNi high-entropy alloy. *J Mater Sci Technol.* 2021;92:195. <https://doi.org/10.1016/j.jmst.2021.02.059>.
- [11] Liu XR, He F, Li JJ, Dang YY, Wang ZJ, Wang JC. Tailoring microstructures of CoCrFeNiNb<sub>0.25</sub> hypoeutectic high-entropy alloy by hot deformation. *Rare Met.* 2022;41(6):2028. <https://doi.org/10.1007/s12598-021-01932-9>.
- [12] Han Y, Li H, Feng H, Tian Y, Jiang Z, He T. Mechanism of dislocation evolution during plastic deformation of nitrogen-doped CoCrFeMnNi high-entropy alloy. *Mater Sci Eng A.* 2021;814: 141235. <https://doi.org/10.1016/j.msea.2021.141235>.
- [13] Tian YZ, Peng SY, Chen SF, Gu ZJ, Yang Y, Shang XL, Deng GY, Su LH, Sun SJ. Temperature-dependent tensile properties of ultrafine-grained C-doped CoCrFeMnNi high-entropy alloy. *Rare Met.* 2022. <https://doi.org/10.1007/s12598-022-01972-9>.
- [14] Kang J, Park N, Kim JK, Park JH. Role of recrystallization and second phases on mechanical properties of (CoCrFeMnNi)<sub>95.2</sub>Al<sub>3.2</sub>Ti<sub>1.6</sub> high entropy alloy. *Mater Sci Eng A.* 2021;814: 141249. <https://doi.org/10.1016/j.msea.2021.141249>.
- [15] Shahmir H, Nili-Ahmadabadi M, Shafiee A, Andrzejczuk M, Lewandowska M, Langdon TG. Effect of Ti on phase stability and strengthening mechanisms of a nanocrystalline CoCrFeMnNi high-entropy alloy. *Mater Sci Eng A.* 2018;725:196. <https://doi.org/10.1016/j.msea.2018.04.014>.
- [16] Kim WJ, Jeong HT, Park HK, Park K, Na TW, Choi E. The effect of Al to high-temperature deformation mechanisms and processing maps of Al<sub>0.5</sub>CoCrFeMnNi high entropy alloy. *J Alloys Compd.* 2019;802:152. <https://doi.org/10.1016/j.jallcom.2019.06.099>.
- [17] Tian YZ, Sun SJ, Lin HR, Zhang ZF. Fatigue behavior of CoCrFeMnNi high-entropy alloy under fully reversed cyclic deformation. *J Mater Sci Technol.* 2019;35:334. <https://doi.org/10.1016/j.jmst.2018.09.068>.
- [18] Haase C, Barrales-Mora LA. Influence of deformation and annealing twinning on the microstructure and texture evolution of face-centered cubic high-entropy alloys. *Acta Mater.* 2018; 150:88. <https://doi.org/10.1016/j.actamat.2018.02.048>.
- [19] Lu Y, Mazilkin A, Boll T, Stepanov N, Zherebtsov S, Salishchev G, Ódor É, Ungar T, Lavernia E, Hahn H, Ivanisenko Y. Influence of carbon on the mechanical behavior and microstructure evolution of CoCrFeMnNi processed by high pressure torsion. *Materialia.* 2021;16:101059. <https://doi.org/10.1016/j.mtla.2021.101059>.
- [20] Li M, Zhang Q, Han B, Song L, Li J, Yang J. Investigation on microstructure and properties of Al<sub>x</sub>CoCrFeMnNi high entropy alloys by ultrasonic impact treatment. *J Alloys Compd.* 2020; 816: 152626. <https://doi.org/10.1016/j.jallcom.2019.152626>.
- [21] Lin PT, Liu HC, Hsieh PY, Wei CY, Tsai CW, Sato YS, Chen SC, Yen HW, Lu NH, Chen CH. Heterogeneous structure-induced strength-ductility synergy by partial recrystallization during friction stir welding of a high-entropy alloy. *Mater Des.* 2021;197:109238. <https://doi.org/10.1016/j.matdes.2020.109238>.
- [22] Oevermann T, Wegener T, Liehr A, Hübner L, Niendorf T. Evolution of residual stress, microstructure and cyclic performance of the equiatomic high-entropy alloy CoCrFeMnNi after deep rolling. *Int J Fatigue.* 2021;153: 106513. <https://doi.org/10.1016/j.ijfatigue.2021.106513>.
- [23] Tong Z, Liu H, Jiao J, Zhou W, Yang Y, Ren X. Microstructure, microhardness and residual stress of laser additive manufactured CoCrFeMnNi high-entropy alloy subjected to laser shock peening. *J Mater Process Technol.* 2020;285: 116806. <https://doi.org/10.1016/j.jmatprotec.2020.116806>.
- [24] Wang C, Jiang C, Zhao Y, Chen M, Ji V. Surface mechanical property and residual stress of peened nickel-aluminum bronze determined by in-situ X-ray diffraction. *Appl Surf Sci.* 2017; 420:28. <https://doi.org/10.1016/j.apsusc.2017.05.108>.
- [25] Zhang J, Li W, Wang H, Song Q, Lu L, Wang W, Liu Z. A comparison of the effects of traditional shot peening and micro-shot peening on the scuffing resistance of carburized and



- quenched gear steel. *Wear*. 2016;368:253. <https://doi.org/10.1016/j.wear.2016.09.029>.
- [26] Jin Y. Annealing twin formation mechanism. Paris: Ecole Nationale Supérieure des Mines de Paris; 2014. 39.
- [27] Okamoto NL, Fujimoto S, Kambara Y, Kawamura M, Chen ZMT, Matsunoshita H, Tanaka K, Inui H, George EP. Size effect, critical resolved shear stress, stacking fault energy, and solid solution strengthening in the CrMnFeCoNi high-entropy alloy. *Sci Rep*. 2016;6:35863. <https://doi.org/10.1038/srep35863>.
- [28] Liu SF, Wu Y, Wang HT, He JY, Liu JB, Chen CX, Liu XJ, Wang H, Lu ZP. Stacking fault energy of face-centered-cubic high entropy alloys. *Intermetallics*. 2018;93:269. <https://doi.org/10.1016/j.intermet.2017.10.004>.
- [29] Zhang HW, Hei ZK, Liu G, Lu J, Lu K. Formation of nanostructured surface layer on AISI 304 stainless steel by means of surface mechanical attrition treatment. *Acta Mater*. 2003;51:1871. [https://doi.org/10.1016/S1359-6454\(02\)00594-3](https://doi.org/10.1016/S1359-6454(02)00594-3).
- [30] Tao NR, Wang ZB, Tong WP, Sui ML, Lu J, Lu K. An investigation of surface nanocrystallization mechanism in Fe induced by surface mechanical attrition treatment. *Acta Mater*. 2002;50:4603. [https://doi.org/10.1016/S1359-6454\(02\)00310-5](https://doi.org/10.1016/S1359-6454(02)00310-5).
- [31] Zhang YH, Zhuang Y, Hu A, Kai JJ, Liu CT. The origin of negative stacking fault energies and nanotwin formation in face-centered cubic high entropy alloys. *Scripta Mater*. 2017;130:96. <https://doi.org/10.1016/j.scriptamat.2016.11.014>.
- [32] Liu J, Chen C, Xu Y, Wu S, Wang G, Wang H, Fang Y, Meng L. Deformation twinning behaviors of the low stacking fault energy high-entropy alloy: an in-situ TEM study. *Scripta Mater*. 2017;137:9. <https://doi.org/10.1016/j.scriptamat.2017.05.001>.
- [33] Xiao J, Wu N, Ojo O, Deng C. Stacking fault and transformation-induced plasticity in nanocrystalline high-entropy alloys. *J Mater Res*. 2021;36:2705. <https://doi.org/10.1557/s43578-021-00140-6>.
- [34] Tao NR, Lu K. Nanoscale structural refinement via deformation twinning in face-centered cubic metals. *Scripta Mater*. 2009;60:1039. <https://doi.org/10.1016/j.scriptamat.2009.02.008>.
- [35] Li X, Wei Y, Lu L, Lu K, Gao H. Dislocation nucleation governed softening and maximum strength in nano-twinned metals. *Nature*. 2010;464:877. <https://doi.org/10.1038/nature08929>.
- [36] Klement W, Willens RH, Duwez POL. Non-crystalline structure in solidified gold-silicon alloys. *Nature*. 1960;187:869. <https://doi.org/10.1038/187869b0>.
- [37] Chen C, Feng XM, Shen YF. Microstructure and mechanical properties of Ti-Cu amorphous coating synthesized on pure Cu substrate by mechanical alloying method. *Rare Met*. 2020;39(10):1222. <https://doi.org/10.1007/s12598-018-1115-x>.
- [38] Xue KM, Zhou YF, Tian WC, Li P. Texture evolution and deformation-induced amorphization in high pressure torsion of W. *Mater Today Commun*. 2020;24: 101178. <https://doi.org/10.1016/j.mtcomm.2020.101178>.
- [39] Qiang J, Tsuchiya K. Concurrent solid-state amorphization and structural rejuvenation in Zr-Cu-Al alloy by high-pressure torsion. *Mater Lett*. 2017;204:138. <https://doi.org/10.1016/j.matlet.2017.06.032>.
- [40] Chen W, Cao S, Zhang J, Zha Y, Hu Q, Sun J. New insights into  $\omega$ -embrittlement in high misfit metastable  $\beta$ -titanium alloys: mechanically-driven  $\omega$ -mediated amorphization. *Mater Des*. 2021;205:109724. <https://doi.org/10.1016/j.matdes.2021.109724>.
- [41] Zhao S, Li Z, Zhu C, Yang W, Zhang Z, Armstrong DEJ, Grant PS, Ritchie PO, Meyers MA. Amorphization in extreme deformation of the CrMnFeCoNi high-entropy alloy. *Sci Adv*. 2021;7:3108. <https://doi.org/10.1126/sciadv.abb3108>.
- [42] Ming K, Lu W, Li Z, Bi X, Wang J. Amorphous bands induced by low temperature tension in a non-equiatom CrMnFeCoNi alloy. *Acta Mater*. 2020;188:354. <https://doi.org/10.1016/j.actamat.2020.02.024>.
- [43] Wang H, Chen D, An X, Zhang Y, Sun S, Tian Y, Zhang Z, Wang A, Liu J, Song M, Ringer SP, Zhu T, Liao X. Deformation-induced crystalline-to-amorphous phase transformation in a CrMnFeCoNi high-entropy alloy. *Sci Adv*. 2021;7:3105. <https://doi.org/10.1126/SCIADV.ABE3105>.
- [44] Kocks UF, Mecking H. Physics and phenomenology of strain hardening: the FCC case. *Prog Mater Sci*. 2003;48:71. [https://doi.org/10.1016/S0079-6425\(02\)00003-8](https://doi.org/10.1016/S0079-6425(02)00003-8).
- [45] Gutierrez-Urrutia I, Raabe D. Dislocation and twin substructure evolution during strain hardening of an Fe-22wt%Mn-0.6wt%C TWIP steel observed by electron channeling contrast imaging. *Acta Mater*. 2011;59:6449. <https://doi.org/10.1016/j.actamat.2011.07.009>.
- [46] Laplanche G, Kostka A, Horst OM, Eggeler G, George EP. Microstructure evolution and critical stress for twinning in the CrMnFeCoNi high-entropy alloy. *Acta Mater*. 2016;118:152. <https://doi.org/10.1016/j.actamat.2016.07.038>.
- [47] Zhu YT, Liao XZ, Wu XL. Deformation twinning in nanocrystalline materials. *Prog Mater Sci*. 2012;57:1. <https://doi.org/10.1016/j.pmatsci.2011.05.001>.
- [48] Sathiyamoorthi P, Kim HS. High-entropy alloys with heterogeneous microstructure: processing and mechanical properties. *Prog Mater Sci*. 2022;123:100709. <https://doi.org/10.1016/j.pmatsci.2020.100709>.
- [49] Li J, Weng GJ, Chen S, Wu X. On strain hardening mechanism in gradient nanostructures. *Int J Plast*. 2017;88:89. <https://doi.org/10.1016/j.ijplas.2016.10.003>.
- [50] Moering J, Ma X, Malkin J, Yang M, Zhu Y, Mathaudhu S. Synergetic strengthening far beyond rule of mixtures in gradient structured aluminum rod. *Scripta Mater*. 2016;122:106. <https://doi.org/10.1016/j.scriptamat.2016.05.006>.
- [51] Ye C, Telang A, Gill AS, Suslov S, Idell Y, Zwiack K, Wiezorek J, Zhou Z, Qian D, Mannava S, Vasudevan V. Gradient nanostructure and residual stresses induced by ultrasonic nano-crystal surface modification in 304 austenitic stainless steel for high strength and high ductility. *Mater Sci Eng A*. 2014;613:274. <https://doi.org/10.1016/j.msea.2014.06.114>.

Springer Nature or its licensor (e.g. a society or other partner) holds exclusive rights to this article under a publishing agreement with the author(s) or other rightsholder(s); author self-archiving of the accepted manuscript version of this article is solely governed by the terms of such publishing agreement and applicable law.